Engineering MoS$_2$ nanomesh with holes and lattice defects for highly active hydrogen evolution reaction

Yue Li[a,1], Kai Yin[c,d,1], Longlu Wang[b,*], Xiaolong Lu[a], Yaqi Zhang[a], Yutang Liu[c,d,**], Dafeng Yan[c], Yuze Song[a], Shenglian Luo[c,d]

[a] School of Materials and Chemical Engineering, Henan Institute of Engineering, Zhengzhou, Henan, 451191, PR China
[b] School of Physics and Electronics, Hunan University, Changsha, 410082, PR China
[c] State Key Laboratory of Chemo/Biosensing and Chemometrics, Hunan University, Changsha, 410082, PR China
[d] College of Environmental Science and Engineering, Hunan University, Changsha, 410082, PR China

ABSTRACT

Molybdenum disulfide (MoS$_2$) presents a promising catalyst to replace state-of the-art platinum (Pt) for hydrogen evolution reaction (HER), but it still lacks an effective way due to the catalytically inert basal plane. Herein, we report a rational design of MoS$_2$ nanomesh that possesses evenly distributed holes and defects to make full use of the 2H-MoS$_2$ basal planes by combining ball-milling with ultrasonic methods. The exfoliation of muti-layer MoS$_2$ to fewer layer or enven monolayer is proceed in pure water without using any chemicals or surfactants. The great advantage of the catalyst is the monolayer, holey and defective structure, which maximizing the synergistic activity for both electrocatalytic and photocatalytic HER performances. Impressively, the MoS$_2$ nanomesh renders outstanding electrocatalytic HER activity with an overpotential of 160 mV at a current density of 10 mV cm^{-2}, and a small Tafel slope of 46 mV decade^{-1}. The photocatalytic H$_2$ evolution rate is about 4.84 mmol h^{-1} when working with Eosin Y as an organic photosensitizer. Additionally, this catalyst shows excellent cycle stability in the electrochemical and photocatalytic reactions. This present work put a new insight into the large-scale production of chemically active 2H MoS$_2$-based catalysts for HER.

1. Introduction

Hydrogen has been widely considered as a clean and renewable energy for replacing petroleum fuels to relieve the energy and environmental crisis [1–10]. To perform the hydrogen evolution reaction (HER), the electrocatalytic HER driven by renewable resource-derived electricity or photocatalytic HER driven by solar-energy photocatalysis are the promising methods [11–13]. Traditionally, these processes require efficient electrocatalyst/cocatalyst to promote the sluggish kinetics. Platinum (Pt) are considered as the most popular catalyst to obtain the top H$_2$ evolution rate, while the high cost and scarcity hampers its wide application in large scale [14–17].

Fortunately, MoS$_2$ with two-dimensional (2D) layered crystal structure exhibit high HER catalytic activities that potentially open a promising new path in this field [18–21]. However, both calculations and experimental results demonstrate that the edges of MoS$_2$ are active but the basal plane is catalytically inert [22]. Since then, considerable efforts have been placed in preparing various MoS$_2$ with the aim that optimizing the active edge sites over the inert basal plane sites, which can be divided into three main techniques: (1) Engineering nanostructured MoS$_2$ to maximally expose edge sites, such as monolayer nanosheets [23], nanodots [24,25], vertical nanoflakes [11,26], porous nanosheets [27] and so on; (2) The introduction of sulfur vacancies on the basal planes to expose under-coordinated edge sites or increase the degree of disorder. The intrinsic activity can be optimized by fine modulating the concentration of S-vacancy [28–30]. Literature has been reported that when 9∼9% S-vacancy are introduced, ΔG$_H$ lies between ± 0.08 eV, which is similar to or better than that of edge sites (0.06 eV) [31,32]; (3) Initiating 2H to 1 T phase transformation or atomic-scale modifications such as chemical doping [33]. However, few approaches have focus on the fully utilization of basal plane directly on the common 2H-MoS$_2$ materials [30,32,34].

At present, the effective routes for the synthesis of monolayer MoS$_2$ nanosheets are chemical exfoliation, chemical vapor deposition (CVD).

We note that liquid phase methods to exfoliate transition metal dichalcogenides (TMDs) using ion intercalation have been known since the1980 s and are experiencing something of a revival today [35,36]. However, such methods are time-consuming, extremely sensitive to environmental conditions. The n-butyllithium that is a dangerous material resulting from the highly pyrophoric property in air is normally required [37,38]. The CVD method incurs high cost and needs high temperature and high vacuum. For defective MoS_2 nanosheets, argon or oxygen plasma exposure and H_2 annealing often apply to controllable create S-vacancy [30,39]. This approach is only effective for flat MoS_2 catalysts and requires high temperature, leading to that it is unsuitable for large-scale synthesis. Therefore, an effective strategy for large-scale preparation of stable 2H-MoS_2 with more active edge sites is still highly desirable.

Ball-milling and direct ultrasonic exfoliation route are facile, cost-efficient, environmental and especially massive production methods [38,40–42]. The ball-milling is a violent process, where the mechanical force originating from the solid–solid reagents would destroy or disorder the crystal structure, leading to reduced layers or defects [42–45]. However, single layer or few-layer nanosheets are hard to obtain though this method. The direct ultrasonic exfoliation route can be used to prepare monolayer or few-layer MoS_2, while this process needs organic solvents with surface tension close to 40 mJ m^{-2}, whose price is high and toxic [40]. Inspired by the above insights, if we use the ball-milling to create S-vacancy in the pristine MoS_2 nanosheets to make the surface tension close to water, the ultrasonic solvent to prepare monolayer or few-layer MoS_2 can be replaced by cheap water [41,45]. Surprisingly, under combining ball-milling and ultrasonic process, the muti-layer MoS_2 were exfoliated to fewer layer or enven monolayer of MoS_2 in pure water without using any chemicals or surfactants. At the same time, S-vacancies and atomic-sized pores were successfully introduced into the basal plane to form the final production of MoS_2 nanomesh. The reduced layers, holey and defect-rich structure of MoS_2 nanomesh synergistic contribute to the more active sites and the fully utilization of basal plane, which are responsible for the further enhanced electrocatalytic and photocatalytic HER activity under visible light irradiation. It is expected that this method can be used to large the scale production of effective 2H-MoS_2 exhibiting high HER activity.

2. Experimental section

2.1. Synthesis of MoS_2 nanosheets

Typically, hexaammonium heptamolybdate tetrahydrate (1 mmol, $(NH_4)6Mo_7O_{24}·4H_2O$, i.e. 7 mmol Mo) and thiourea (30 mmol) were dissolved in deionized water (35 mL) under vigorous stirring to form a homogeneous solution. Then, the solution was transferred into a 45 ml Teflon-lined stainless steel autoclave and maintained at 220 °C. After 18 h, the reaction system was allowed to cool to room temperature. The final product was washed with water and absolute ethanol for several times to remove any possible ions, and dried at 60 °C under vacuum.

2.2. Synthesis of defective MoS_2 nanosheets

The mechanical activated MoS_2 was prepared by ball-milling in a high-energy planetary mill with stainless steel balls as milling media (ball-to-powder weight ratio—18:1). The milling was performed at 400 rpm for 24 h in an atmosphere of argon.

2.3. Synthesis of MoS_2 nanomesh

Defective MoS_2 nanosheets was added into a 120 ml titanium container filled with water for ultrasound irradiation. Subsequently, the titanium container was sealed under air atmosphere and kept in a circulating water bath to maintain the temperature of bulk solution at 20 ± 5 °C. The solution was irradiated with high-intensity ultrasound

for 6 h. The final black precipitates were collected, washed with distilled water, absolute ethanol and ammonia in turn for several times, and then dried in vacuum at 40 °C for 10 h.

2.4. Characterization

The morphology and structure of the as-prepared materials were characterized via field emission scanning electron microscopy (SEM, Hitachi S-4800), transmission electron microscopy (TEM, JEM-3010), high angle annular dark field-scanning TEM (HAADF-STEM, FEI Tecnai G2 F20 S-TWIN) and atomic force microscopy (AFM) on a Veeco DI Nano-scope MultiMode V system. The crystal phases of the samples were collected on an X-ray diffractometer with Cu-K radiation (XRD, M21X, MAC Science Ltd., Japan). X-ray photoemission spectroscopy (XPS) was measured on a Thermo Fisher Scientific Escalab 250Xi system with a monochromatic Al Kα source. Electron spin resonance (ESR) were performed on a Bruker ER 200D spectrometer at room temperature with 28 mg of each sample, which was loaded into a quartz tube. The microwave frequency was maintained in the range of 9.8591–9.8599 GHz (X-band), and the microwave power was fixed at 20 mW to avoid saturation. The UV/Vis diffuse reflectance spectra (DRS) were recorded on a UV/Vis spectrophotometer (Cary300, USA) with an integrating sphere.

2.5. Electrochemical and photoelectrochemical measurements

All electrochemical and photoelectrochemical measurements were conducted at room temperature on a standard three-electrode electrolytic system with saturated calomel electrode (SCE) as reference electrode, Pt as counter electrode and glass carbon deposited with catalyst sample as working electrode. The HER activities were conducted by linear sweep voltammetry (LSV) solution with a scan rate of 5 mV s^{-1}. The long-term stability was tested by taking continuous cyclic voltammograms at a scan rate of 50 mV s^{-1} from —0.4 V to 0.1 V with 1000 cycles. The striking stability was further proved by using chronoamperometry (j ~ t) at 180 mV. All the measurements were performed in 0.5 M H_2SO_4 without IR compensated. The working electrode was prepared by drop the catalyst aqueous solution onto glass carbon electrode. The samples were dispersed in water at 1 mg/ml directly. Then 20 μl was deposited on the working electrode (equivalent to 0.28 mg/cm^2). If no special emphasis, all the potentials were here referenced to the reversible hydrogen electrode (RHE) using the following equation: E(RHE) = E(SCE) + 0.24 V + 0.059 × pH. The photocurrent response of photocatalyst samples were measured in a mixed solution of TEOA (15 vol %) and 0.1 M Na_2SO_4. The working electrodes were prepared by drop-coating sample suspensions (1 mg/mL) directly onto the ITO glass surface, the surface exposed to the electrolyte was about 1.6 cm^2. A 300 W xenon arc lamp with a UV cut-off filter (λ > 420 nm) was used for excitation

2.6. Photocatalytic hydrogen production

Photocatalytic H_2 production experiments were carried out in a 100 ml sealed quartz reactor. The light source was a 300 W xenon arc lamp with a UV cut-off filter (λ > 420 nm) (Perfect light, PLS-SXE 300C, Beijing, China). The produced H_2 was measured by gas chromatography (GC2010, Shimadzu) equipped with a thermal conductivity detector (TCD) and a 5 A molecular sieve column. The catalyst (20 mg) was dispersed in a 80 ml aqueous solution containing triethanolamine (TEOA) (15%, v/v) and Eosin Y (EY) dye (20 mg) with stirring at pH 7. Before reaction, the system was thoroughly degassed by bubbling nitrogen for 15 min. All the reactions were kept at room temperature by using cooling water.
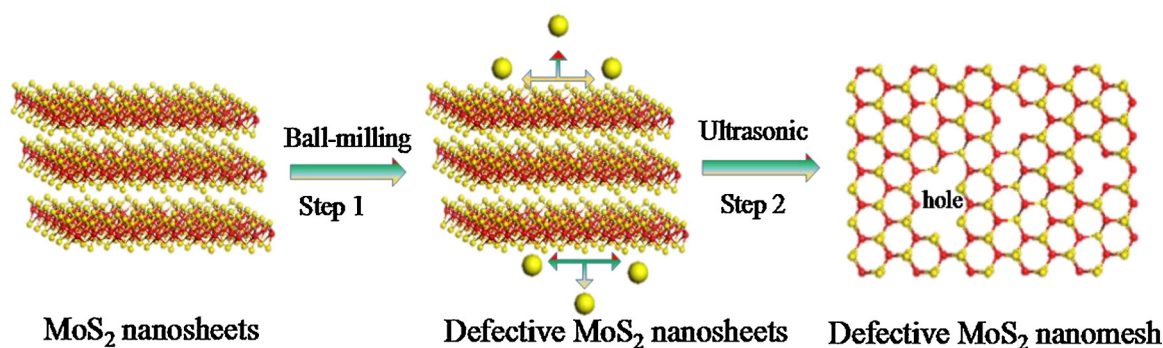
Fig. 1. Schematic illustration of fabrication of monolayer MoS$_2$ nanomesh with defective atomic-sized pores in the basal plane for amplifying HER catalysis.

3. Results and discussion

3.1. Formation of the defective MoS$_2$ nanomesh

A schematic overview of the synthesis procedure is shown in Fig. 1. Since the ball milling treatment is a violent process which cleaves the raw materials from both vertical and horizontal direction, the defects (S-vacancies) could be created in hydrothermal synthesis of MoS$_2$ nanosheets, as a result in the surface tension of pristine MoS$_2$ is changed (step 1). Then, under the irradiation of ultrasonic, the defective MoS$_2$ is sheared into monolayer MoS$_2$ with many holes in water as MoS$_2$ nanomesh (step 2). The atomic-scale holes on the basal planes of monolayer MoS$_2$ may be caused by the defects (S-vacancies) in MoS$_2$. Actually, the energy for removing sulphur atoms in a perfect MoS$_2$ nnaosheet is calculated by first-principles calculations to be 6.1 eV, whereas the data is significantly reduced to 4.9 or 4.4 eV from an armchair or zigzag edge [46]. Therefore, the sulphur atoms at the edge of MoS$_2$ nanosheets are too fragile to withstand the ultrasound irradiation. When the beam energy exceeds the knock-on damage threshold of the nanosheets, it's easier for the defects MoS$_2$ nanosheets to form pinholes [47,48]. Once the pinholes are created, the dangling bonds within them prefer to enlargement of a single nanopore rather than nucleation of many pores, as a result in forming the final production of MoS$_2$ nanomesh. The lower coordination number, more dangling bonds and more obvious structural distortion enable the hole edge sites to act as the most favorable active sites to tailor the catalytic performance.

3.2. Characterization supports of catalysts

The morphologies of the samples were obtained from transmission electron microscopy (TEM) and high-resolution TEM (HRTEM) images. Fig. 2a displays the MoS$_2$ nanosheets have obvious complete nanosheets with corrugated edges. The layers of the MoS$_2$ nanosheets are about 7 layers (Inset of Fig. 2a). After the ball-milling and ultrasonic processes, the entire MoS$_2$ nanosheets were crushed and sheared into small pieces, and some atomic-scale holes were configured in the basal planes of monolayer MoS$_2$ whose morphology looks like MoS$_2$ nanomesh (Fig. 2b). The fewer layers or even monolayer structure of MoS$_2$ nanomesh is shown in Fig. 2c by the arrows. Simultaneously, AFM was used to further confirm the fewer layers or monolayer structure of MoS$_2$ nanomesh, as shown in Fig. 2h. The monolayer and holes allow more active edge sites and activated basal planes, which are expected to boost the intrinsic HER activity of 2H-MoS$_2$ [17,22]. The element mapping Mo and S (Fig. 2e and f) of HAADF-STEM image of the MoS$_2$ nanomesh (Fig. 2d) and EDS spectrum (Fig. 2g) of MoS$_2$ nanomesh confirm the composition is Mo and S. The uniform color and luster of element mapping means homogeneous dispersion of S or Mo.

The precise microscopic knowledge of defect atomic structure is of fundamental importance. To obtain an atomistic understanding the structure of the prepared samples, we performed HRTEM analysis of the pristine MoS$_2$ and MoS$_2$ nanomesh. As shown in Fig. 3a b and d e, the

atomic arranging manner on the basal surface is strongly disordered after ball-milling and ultrasonic processes, even short-range ordering of nanodomains could not be clearly observed. That is because these clusters and atoms are highly mobile and prone to form a disordered structure of MoS$_2$ in the lowest total energy. The degree of disorder can be evaluated by the angle which determined by two endpoints of a diffraction arc and the central spot [49], as shown in corresponding FFT patterns (Fig. 3c and f). That is, the angle of 60° represents completely disordered atomic arrangement, while 0° represents perfect single crystal without disordering. The obvious evolution of the degree indicates that the pristine MoS$_2$ nanosheets have perfect crystal while the MoS$_2$ nanomesh has completely disordered atomic arrangement. The disordered structure makes the MoS$_2$ nanomesh more stable, and there are more dangling bonds available to provide active sites for higher HER performance [49].

The XRD patterns were used to identify the interlayer spacing and phase change of MoS$_2$ nanosheets and defective MoS$_2$ nanomesh. As shown in Fig. 4a, all the detected peaks are assigned to hexagonal phase MoS$_2$, among which the (002) peak centered at 14.4° illustrates the stacking level of MoS$_2$ nanosheets. Based on JADE crystal phase analysis for XRD data, the peak area ratio of (002)/(100) decrease from 3.0 to 1.0. A lower proportion of crystal phase (002) means a reduced number of aligned planes [8,12,26]. Obviously, the stacked layers along the c axis were destroyed after the ball milling and ultrasonic processes, indicating that the MoS$_2$ nanostructures were efficiently converted into fewer layer or single layers of MoS$_2$. This result is in good agreement with HRTEM image of Fig. 2c which shows the fewer layers or monolayer structure of defective MoS$_2$ nanomesh.

XPS measurements were conducted to characterize the surface compositions and whether the S-vacancies were introduced after ball-milling and ultrasonic processes. As shown in Fig. 4b, the pristine MoS$_2$ features two characteristic peaks at around 229.3 and 232.7 eV, corresponding to Mo^{4+} 3d$_{5/2}$ and Mo^{4+} 3d$_{3/2}$ components, respectively. Simultaneously, the peak at 226.2 eV belongs to S 2 s orbital of MoS$_2$. In S 2p region of the spectra (Fig. 4c), the peaks located at 161.6 and 162.7 eV are assigned to S 2p$_{3/2}$ and 2p$_{1/2}$, respectively. For the MoS$_2$ nanomesh, as shown in Fig. 4d and e, Mo 3d peaks and S 2p peaks for the defective MoS$_2$ nanomesh are much weaker than those of MoS$_2$ nanosheets [50]. Specially the normalized S/Mo ratio is reduced from 2.01 of stoichiometric MoS$_2$ nanosheets to 1.85 of defective MoS$_2$ nanomesh (1.99 to 1.85 for ICP), as shown in Table S1. The results suggest that the loss of the S element, resulting in approximately 9.5% S-vacancies. The electron spin resonance (ESR) reveals the S signal intensity of defective MoS$_2$ nanomesh is significantly lower than that of MoS$_2$ nanosheets, which further confirms the formation of S-vacancies (Fig. 4f).

From the above discussion, the novel MoS$_2$ nanomesh can significantly increase the exposure of active edge sites due to the reduced layers and the formation of defects and holes on the basal surface. This conclusion can be further confirmed by the zeta (ζ) potentials in aqueous solution. A more negative ζ-potential means the catalyst can
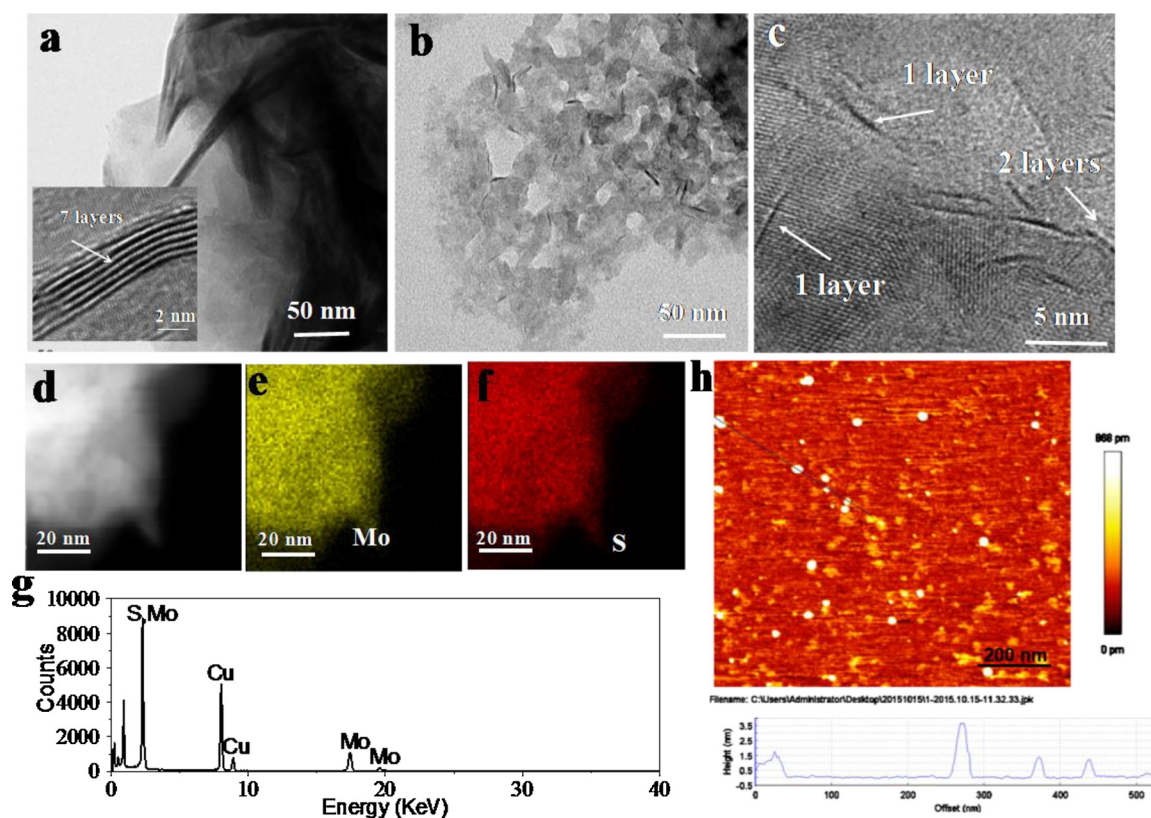
Fig. 2. TEM images of (a) pristine MoS$_2$ nanosheets and (b) MoS$_2$ nanomesh. Inset of (a) shows the layers of the MoS$_2$ nanosheets. (c) HRTEM image of the MoS$_2$ nanomesh, which reveals the monolayer structure. (d–f) Element mapping and (g) EDS spectrum of the MoS$_2$ nanomesh. (h) AFM image of the MoS$_2$ nanomesh.

provide more active sites for the reduction of protons to generate H$_2$ [51]. As shown in Fig. 5a, the MoS$_2$ nanomesh reveals more negative ζ-potentials than the defective MoS$_2$ nanosheets and MoS$_2$ nanosheets in the pH range 2–12. That is to say, an increased exposure edge sites and S-vacancies are existed on the defective MoS$_2$ nanomesh, which allow to achieve an enhanced HER efficiency.

Besides the exposed active edge sites, high electric conductivity and hydrophilic surface can stand the catalyst in good stead for outstanding HER performances. Fig. 5b shows the Nyquist plots of the samples, the smallest semicircle of MoS$_2$ nanomesh demonstrates the highest conductivity, meaning an enhanced charges transport rate between the MoS$_2$ edges and electrolyte [12]. Contact angle measurements can be
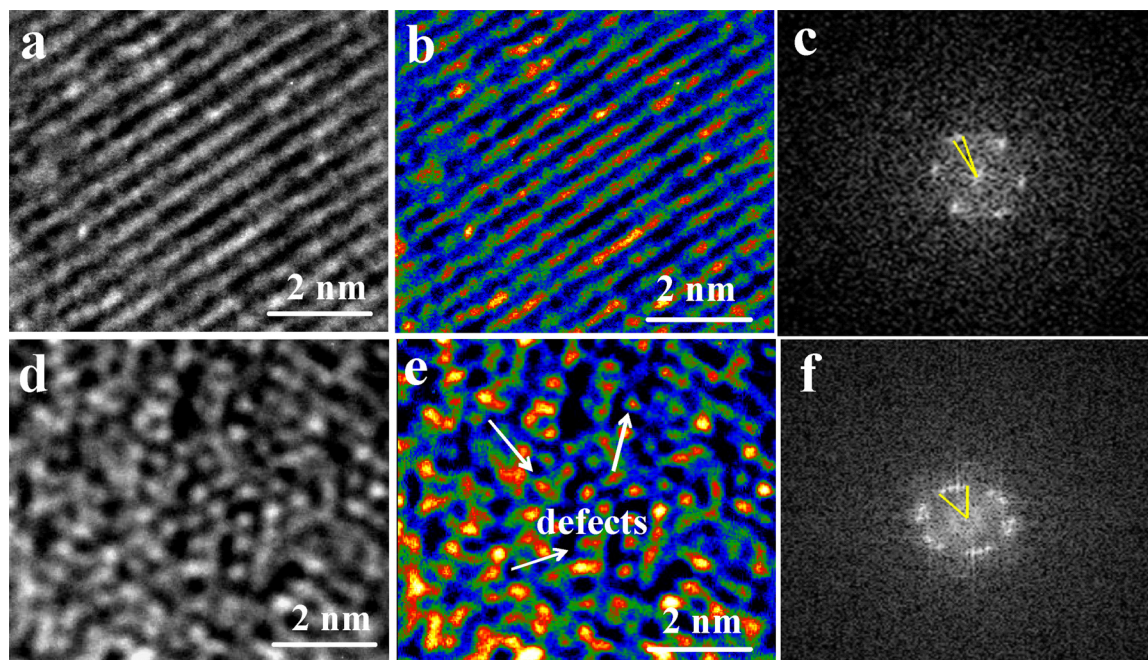

Fig. 3. HRTEM images of (a) MoS$_2$ nanoheets and (b) MoS$_2$ nanomesh. (b, e) are false–color images responding to (a, d), respectively. (c, f) were FFT images responding to (a, d), respectively.
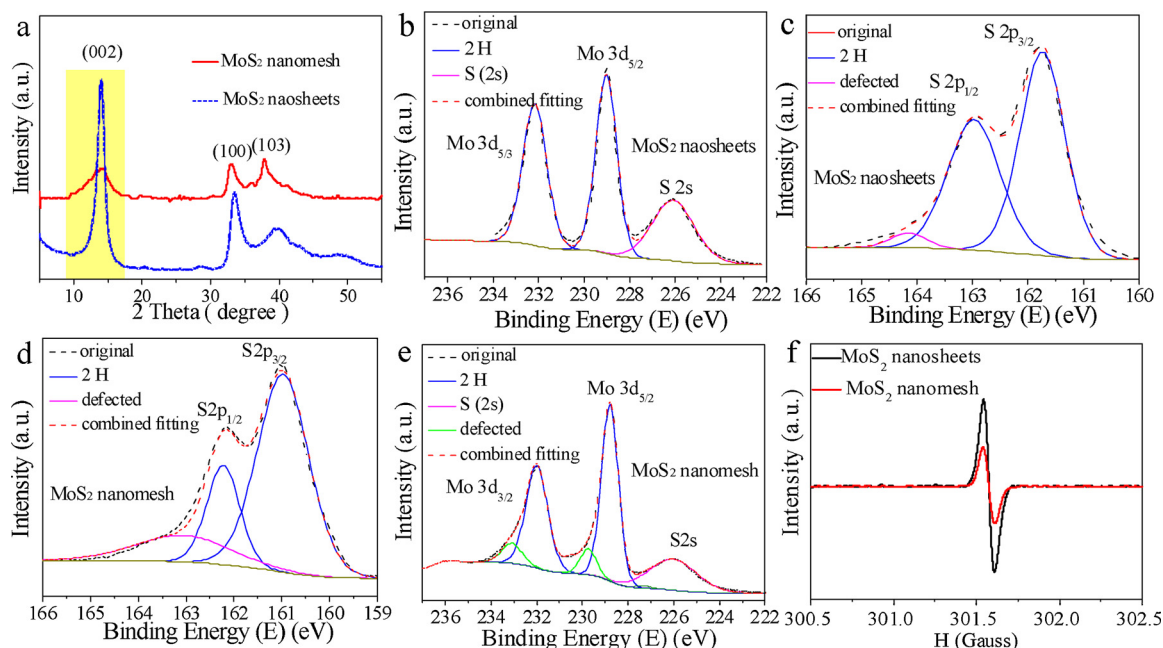
Fig. 4. (a) XRD patterns of the as-prepared MoS₂ nanoheets and MoS₂ nanomesh. XPS spectra of Mo 3d and S 2p binding energies of pristine MoS₂ nanosheets (b and c, respectively) and defective MoS₂ nanomesh (d and e, respectively). (f) Electron spin resonance spectra for MoS₂ nanosheets and MoS₂ nanomesh. The annealing experiment was under Ar atmosphere at 300 °C for 2 h.
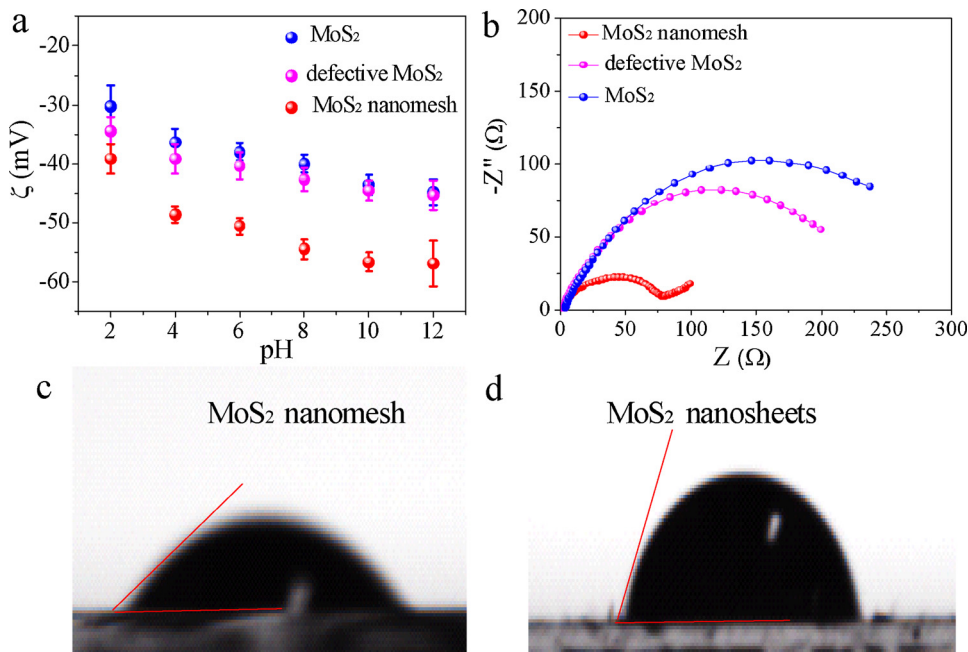

Fig. 5. (a) Zeta (ζ) potentials of MoS₂ nanosheets, defective MoS₂ nanosheets and MoS₂ nanomesh as a function of pH in aqueous dispersions. (b) Nyquist plots of MoS₂ nanosheets, defective MoS₂ nanosheets and MoS₂ nanomesh at a HER overpotential of 200 mV. Static contact angle images of (c) MoS₂ nanomesh and (d) MoS₂ nanosheets.

used to detect the hydrophilicity and hydrophobicity of the samples. The smaller the angle is, the better the hydrophilicity is [34,52]. As shown in Fig. 5c and d, contact angles of 30° and 75° are observed on MoS₂ nanomesh and MoS₂ nanosheets, respectively. The lower contact angle suggests the highly hydrophilic surface of MoS₂ nanomesh, which would favorable for more efficient hydrogen production by electrolytes can better adsorb on the catalyst.

3.3. Excellent electrochemical HER efficiency

In order to verify our expectation, the electrocatalytic activities of the catalysts for HER were measured in a conventional three-electrode system with a scan rate of 5 mV s⁻¹. As shown in Fig. 6a, the MoS₂

nanomesh exhibits the best catalytic activity with a low overpotential of 160 mV (V vs RHE), compared to the overpotential of 230 mV for MoS₂ nanosheets and 208 mV for defective MoS₂ nanosheets at 10 mA cm⁻². It indicates that the defective atomic-sized pores in the basal planes of MoS₂ nanomesh can significantly increase the electrochemical HER activity. The corresponding Tafel slopes derived from the polarization curves are shown in Fig. 6b. A lower Tafel slope means a more efficient kinesis of H₂ evolution at a constant increase of overpotential. The MoS₂ nanomesh displays a Tafel slope of 46 mV·dec⁻¹, which is smaller than those of other catalysts except for the state-of-the-art Pt/C catalyst. To the best of our knowledge, our synthetic defective MoS₂ nanomesh here is the most efficient MoS₂ with 2H phase in the reported literature (Table S2). On the basis of general mechanisms for the electrochemical
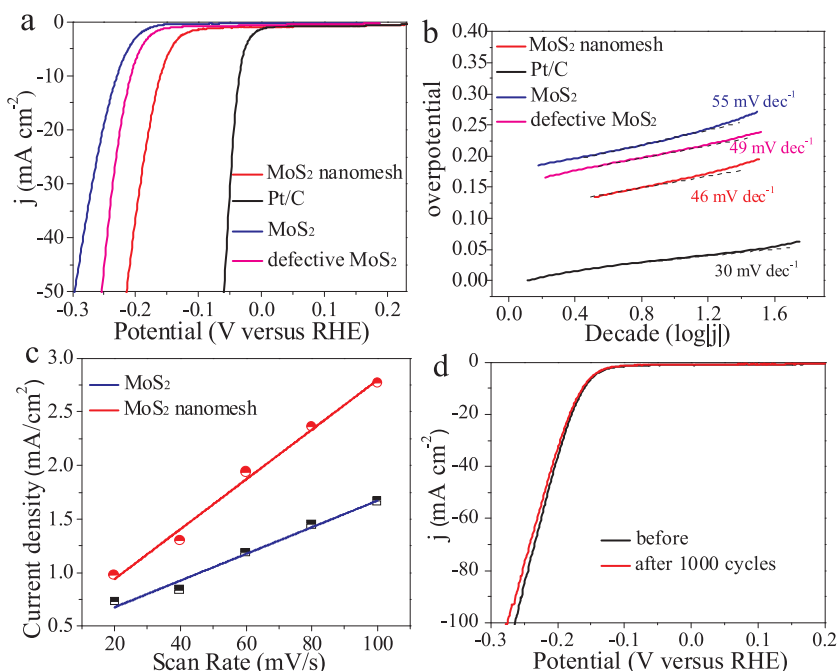
Fig. 6. (a) Polarization curves and (b) corresponding Tafel slopes of Pt, MoS_2 nanosheets, defective MoS_2 nanosheets and MoS_2 nanomesh in 0.5 M H_2SO_4 at a scan rate of 5 mV. (c) Double-layer capacitance (Cdl) for MoS_2 nanosheets and defective MoS_2 nanomesh.(d) Durability test for defective MoS_2 nanomesh before and after 1000 cycles.

HER process, the Tafel slope of 46 mV·dec^{-1} for the MoS_2 nanomesh implies a Volmer-Heyrovsky mechanism [53].

The double-layer capacitance (Cdl) can be used to evaluate the effective electrochemical active surface area, which is another important factor affecting the rate of electrochemical H_2 production. In particularly, cyclic voltammograms (CVs) were collected in the region of $0 - 0.1$ V, where the current response should only attribute to the charging/discharging of electric double layer (Fig. S1). As shown in Fig. 6c,the capacitance of 8.5 m F cm^{-2} for MoS_2 nanomesh is larger than that of MoS_2 nanosheets (4.1 m F cm^{-2}), further explaining the best electrochemical HER activity was achieved on the MoS_2 nanomesh.

Durability is another significant criterion for HER catalysts. Continuous cyclic voltammetry before and after application of 1000 cycles were performed to investigate the stability of MoS_2 nanomesh (Fig. 6d). There is almost no loss of cathodic current compared to the first cycle, illustrating an ultrahigh stability under the repeated cycles. Fig. S2 further indicates the durability of MoS_2 nanomesh by the constant voltage technique at overpotential of 180 mV. Negligible loss of current density can be observed even after a long period of 10 h.

3.4. Excellent photocatalytic HER efficiency

Fig. 7a reveals the time courses of H_2 evolution catalyzed by MoS_2 nanosheets, defective MoS_2 nanosheets, and MoS_2 nanomesh using Eosin Y (EY) as the photosensitizer and triethanolamine (TEOA) as the sacrificial reagent under visible light irradiation (≥ 420 nm). It can be clearly seen that all the samples can efficiently generate H_2, suggesting that the MoS_2 itself could also work well as a cocatalyst in a dye-sensitization based photochemical system. The rate of H_2 evolution increased significantly to 4.84 mmol h^{-1} for the MoS_2 nanomesh, which is about 5.97 times higher than that of the MoS_2 nanosheets (0.81 mmol h^{-1}), and 2.41 times higher than that of defective MoS_2 nanosheets (1.86 mmol h^{-1}) under the same conditions. Furthermore, the H_2 evolution rate of the MoS_2 nanomesh is very stable during long-term test (Fig. 7b). Even after 30 h, the H_2 generation rate in the sixth cycle remains nearly the same in the first cycle, demonstrating the MoS_2 nanomesh is a high-performance photocatalyst for photocatalytic HER.

The H_2 evolution efficiency is relate to the electron transfer behavior which can be confirmed by the moderated fluorescence quenching of EY in the presence of different catalysts. A high photoluminescence is

origin from a relaxation process which is unfavorable to the production of H_2 [54]. As shown in Fig. 7c, the fluorescence emission decays of the EY with the order of the pure EY $<$ the MoS_2 nanosheets/EY $<$ the defective MoS_2 nanosheets/EY $<$ the MoS_2 nanomesh/EY. The introduction of S-vacancies on the defective MoS_2 nanosheets increase the active site density, resulting in the rapid transfer of photogenerated electrons from EY to the MoS_2 nanosheets. When the atomic-scale holes were created on the monolayer MoS_2 nanomesh, the photogenerated electrons transfer rate on the MoS_2 nanomesh/EY was further enhanced. The fast electrons transfer rate can efficiently suppress the relaxation process, thus accounting for the lowest photoluminescence and highest H_2 evolution activity on the MoS_2 nanomesh/EY. It also can be confirmed by photoelectrochemical experiments [55]. Fig. 7d revels dramatically enhancement in photocurrent of MoS_2 nanomesh in relative to the MoS_2 nanosheets/EY and the defective MoS_2 nanosheets/ EY, further indicating the improved interfacial electron transfer from EY to MoS_2 nanomesh. Fig. S3 shows the UV/Vis diffuse reflectance spectra of MoS_2 nanosheets and MoS_2 nanomesh. The MoS_2 nanosheets exhibit a smooth curve without specific absorption peak, while the MoS_2 nanomesh has a strong absorption from 600 nm to 700 nm. This implies the characteristic feature of MoS_2 nanomesh has fewer layer or even monolayer. A plot of the transformed Kubelka $-$ Munk function versus photon energy reveals that the band gap of MoS_2 nanomesh is bigger than the MoS_2 nanosheets, further indicating the MoS_2 nanomesh has much fewer layers with more active edge sites. As a result, the highest photocatalytic H_2 evolution activity was obtained on the MoS_2 nanomesh, which may be attributed to the synergetic effect of monolayer, atomic-scale holes and S-vacancies.

3.5. The speculation of mechanism for H_2 evolution

In principle, the high photocatalytic water splitting performance is related to many factors, such as more active areas, superior electrical conductivity, faster charge transfer rate, lower Gibbs free energy of adsorbed hydrogen (ΔG_H), and so on [23,32,34,42]. The prepared MoS_2 nanomesh exhibits both the highest electrochemical and photocatalytic HER efficiency due to the above synergetic effects which derived from the reduced layers and the defective atomic-scale holes on the basal plane (Fig. 8). This excellent structure is specifically shown in the following four aspects: First of all, the combination of exposing more
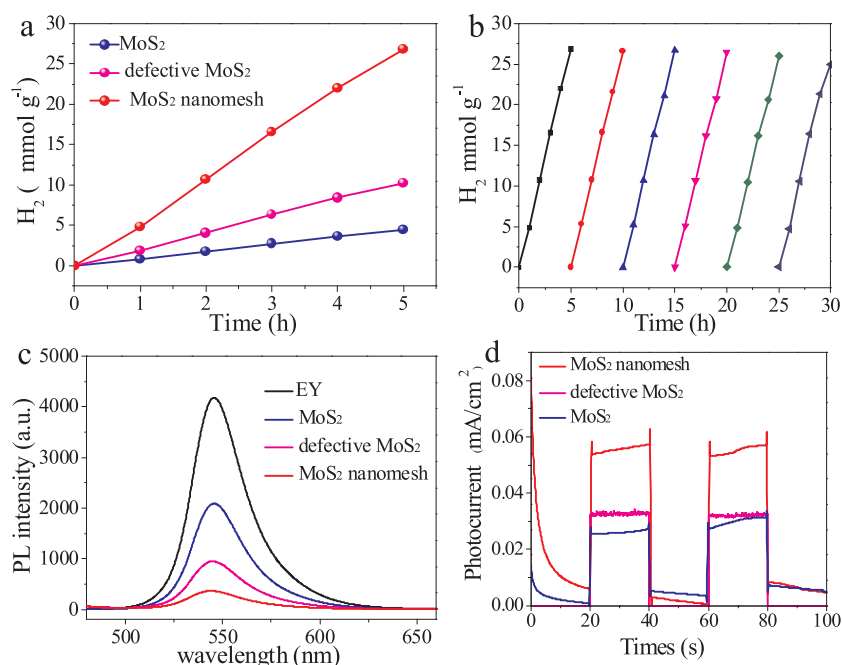
active sites with activating basal plane can stimulate the HER activity. Second, the improved conductivity enhances the electron transport rate as a result in accelerating the rate of H_2 production. Third, the introduction of sulfur vacancies reduces the ΔG_H value on the active site, making it much closer to the Pt. Fourth, the MoS_2 nanomesh is superhydrophilic, it is more favorable to water to access and penetrate. All of the above factors lead to the highest electrochemical and photocatalytic HER efficiency.

Furthermore, the detail mechanism of photocatalytic H_2 production on the MoS_2 nanomesh is given in Fig. 8. After the absorption of light by EY, the EY dye molecules transform into singlet excited state (EY^{1*}), and then produce the lowest-lying triplet excited-state EY^{3*} via an efficient intersystem crossing (ISC) [55]. The oxidation EY^{3*} can be reductively quenched by sacrificial donor TEOA to form $EY^{-\cdot}$. The electrons of $EY^{-\cdot}$ are transferred to the MoS_2 nanomesh, and then reduce the absorbed H_2O to generate H_2. The literature reported that only the metallic edges of 2H-MoS_2 are catalytically active but the basal planes are inert [56]. Thus, the electrons transfer from $EY^{-\cdot}$ to the MoS_2 nanomesh are easier than the MoS_2 nanosheets and defective MoS_2

nanosheets due to above discussed synergetic factors, leading to the highest HER efficiency on the MoS_2 nanomesh.

4. Conclusions

In summary, we developed a facile ball-milling combined ultrasonic method to fabricate MoS_2 nanomesh without using any toxic chemicals or surfactants. Due to the synergistic effects of monolayer, atomic-scale holes and S-vacancies, the MoS_2 nanomesh exhibits increased number of active edge sites, improved conductivity, and stronger hydrogen adsorption ability. As a result, the unique structure significantly improves the electrochemical and photocatalytic HER activity compared with the MoS_2 nanosheets and the defective MoS_2 nanosheets. Particularly, a low overpotential of 160 mA cm^{-2} mV (V vs RHE) at 10 mA cm^{-2} and a small Tafel slope of 46 mV $decade^{-1}$ are achieved for the electrochemical HER. It also exhibits a high initial photocatalytic H_2 evolution rate of 4.84 mmol h^{-1} over the EY-sensitized MoS_2 nanomesh. Furthermore, excellent long-term stability in the electrochemical and photocatalytic reactions are also achieved on the MoS_2 nanomesh.
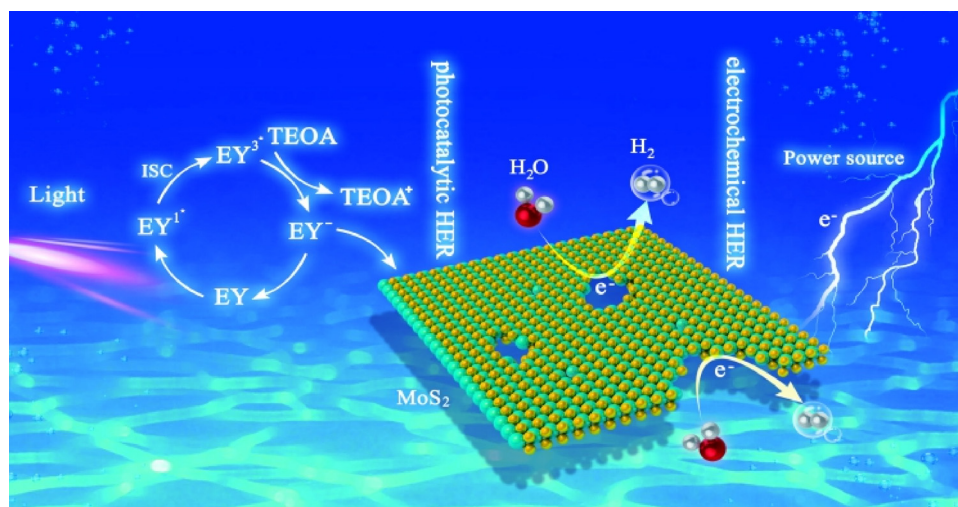

Fig. 8. Electrochemical and photocatalytic mechanism for H_2 evolution over the unique MoS_2 nanomesh.

This study describes a novel and effective route for activating basal planes of layered 2D nanomaterials as promising alternatives for Pt in HER applications.

Acknowledgements

Appendix A. Supplementary data

Supplementary material related to this article can be found, in the online version, at doi:https://doi.org/10.1016/j.apcatb.2018.05.080.

References

[1] D.P. Kumar, S. Hong, D.A. Reddy, T.K. Kim, Appl. Catal. B Environ. 212 (2017) 7–14.
[2] D. Voiry, M. Salehi, R. Silva, T. Fujita, M. Chen, T. Asefa, V.B. Shenoy, G. Eda, M. Chhowalla, Nano Lett. 13 (2013) 6222–6227.
[3] X. Zong, H. Yan, G. Wu, G. Ma, F. Wen, L. Wang, C. Li, J. Am. Chem. Soc. 130 (2008) 7176–7177.
[4] Y. Li, X. Wei, B. Zhu, H. Wang, Y. Tang, T.C. Sum, X. Chen, Nanoscale 8 (2016) 11284–11290.
[5] B. Han, S. Liu, N. Zhang, Y.-J. Xu, Z.-R. Tang, Appl. Catal. B Environ. 202 (2017) 298–304.
[6] N. Shao, J. Wang, D. Wang, P. Corvini, Appl. Catal. B Environ. 203 (2017) 964–978.
[7] M. Li, L. Zhang, X. Fan, M. Wu, Y. Du, M. Wang, Q. Kong, L. Zhang, J. Shi, Appl. Catal. B Environ. 190 (2016) 36–43.
[8] N. Shao, Z. Hou, H. Zhu, J. Wang, C.P. François-Xavier, Appl. Catal. B Environ. 232 (2018) 574–586.
[9] L. Wang, X. Duan, G. Wang, C. Liu, S. Luo, S. Zhang, Y. Zeng, Y. Xu, Y. Liu, X. Duan, Appl. Catal. B Environ. 186 (2016) 88–96.
[10] Y. Li, X. Wei, X. Yan, J. Cai, A. Zhou, M. Yang, K. Liu, Phys. Chem. Chem. Phys. 18 (2016) 10255–10261.
[11] Y. Li, L. Wang, T. Cai, S. Zhang, Y. Liu, Y. Song, X. Dong, L. Hu, Chem. Eng. J. 321 (2017) 366–374.
[12] Y. Li, L. Wang, S. Zhang, X. Dong, Y. Song, T. Cai, Y. Liu, Catal. Sci. Technol. 7 (2017) 718–724.
[13] Y. Li, J. Feng, H. Li, X. Wei, R. Wang, A. Zhou, Int. J. Hydrogen Energy 41 (2016) 4096–4105.
[14] M.-R. Gao, M.K.Y. Chan, Y. Sun, Nat. Commun. 6 (2015) 7493.
[15] Y. Yin, J. Han, Y. Zhang, X. Zhang, P. Xu, Q. Yuan, L. Samad, X. Wang, Y. Wang, Z. Zhang, J. Am. Chem. Soc. 138 (2016) 7965–7972.
[16] G. Zhang, H. Liu, J. Qu, J. Li, Energy Environ. Sci. 9 (2016) 1190–1209.
[17] X.-H. Zhang, N. Li, J. Wu, Y.-Z. Zheng, X. Tao, Appl. Catal. B Environ. 229 (2018) 227–236.
[18] Z. Liu, Z. Gao, Y. Liu, M. Xia, R. Wang, N. Li, ACS Appl. Mater. Interfaces 9 (2017) 25291–25297.
[19] Q. Liu, Q. Fang, W. Chu, Y. Wan, X. Li, W. Xu, M. Habib, S. Tao, Y. Zhou, D. Liu, T. Xiang, A. Khalil, X. Wu, M. Chhowalla, P.M. Ajayan, L. Song, Chem. Mater. 29 (2017) 4738–4744.
[20] Y. Chen, G. Tian, Y. Shi, Y. Xiao, H. Fu, Appl. Catal. B Environ. 164 (2015) 40–47.
[21] X. Meng, Z. Li, H. Zeng, J. Chen, Z. Zhang, Appl. Catal. B Environ. 210 (2017) 160–172.
[22] X. Hai, W. Zhou, S. Wang, H. Pang, K. Chang, F. Ichihara, J. Ye, Nano Energy 39 (2017) 409–417.
[23] S. Su, Q. Zhou, Z. Zeng, D. Hu, X. Wang, M. Jin, X. Gao, R. Nötzel, G. Zhou, Z. Zhang, J. Liu, ACS Appl. Mater. Interfaces 10 (2018) 8026–8035.
[24] C. Han, Y. Zhang, P. Gao, S. Chen, X. Liu, Y. Mi, J. Zhang, Y. Ma, W. Jiang, J. Chang, Nano Lett. 17 (2017) 7767–7772.
[25] X. Hao, Z. Jin, H. Yang, G. Lu, Y. Bi, Appl. Catal. B Environ. 210 (2017) 45–56.
[26] C. Liu, L. Wang, Y. Tang, S. Luo, Y. Liu, S. Zhang, Y. Zeng, Y. Xu, Appl. Catal. B Environ. 164 (2015) 1–9.
[27] W. Zhou, K. Zhou, D. Hou, X. Liu, G. Li, Y. Sang, H. Liu, L. Li, S. Chen, ACS Appl. Mater. Interfaces 6 (2014) 21534–21540.
[28] H. Li, M. Du, M.J. Mleczko, A.L. Koh, Y. Nishi, E. Pop, A.J. Bard, X. Zheng, J. Am. Chem. Soc. 138 (2016) 5123–5129.
[29] A.Y. Lu, X. Yang, C.C. Tseng, S. Min, S.H. Lin, C.L. Hsu, H. Li, H. Idriss, J.L. Kuo, K.W. Huang, L.J. Li, Small 12 (2016) 5530–5537.
[30] C. Tsai, H. Li, S. Park, J. Park, H.S. Han, J.K. Nørskov, X. Zheng, Nat. Commun. 8 (2017) 15113.
[31] C. Tsai, F. Abild-Pedersen, J.K. Nørskov, Nano Lett. 14 (2014) 1381–1387.
[32] H. Li, C. Tsai, A.L. Koh, L. Cai, A.W. Contryman, A.H. Fragapane, J. Zhao, H.S. Han, H.C. Manoharan, F. Abild-Pedersen, J.K. Nørskov, X. Zheng, Nat. Mater. 15 (2015) 48.
[33] L. Wang, X. Liu, J. Luo, X. Duan, J. Crittenden, C. Liu, S. Zhang, Y. Pei, Y. Zeng, X. Duan, Angew. Chem. Int. Ed. 56 (2017) 7610–7614.
[34] X. Huang, M. Leng, W. Xiao, M. Li, J. Ding, T.L. Tan, W.S.V. Lee, J. Xue, Adv. Funct. Mater. 27 (2017) 1604943.
[35] L. Wang, Q. Zhang, J. Zhu, X. Duan, Z. Xu, Y. Liu, H. Yang, B. Lu, Energy Storage Mater. 16 (2018) 37–45.
[36] Q. Zhang, L. Wang, J. Wang, X. Yu, J. Ge, H. Zhang, B. Lu, J. Mater. Chem. A 6 (2018) 9411–9419.
[37] A. Ciesielski, P. Samori, Chem. Soc. Rev. 43 (2014) 381–398.
[38] X. Hai, K. Chang, H. Pang, M. Li, P. Li, H. Liu, L. Shi, J. Ye, J. Am. Chem. Soc. 138 (2016) 14962–14969.
[39] G. Ye, Y. Gong, J. Lin, B. Li, Y. He, S.T. Pantelides, W. Zhou, R. Vajtai, P.M. Ajayan, Nano Lett. 16 (2016) 1097–1103.
[40] X. Fan, P. Xu, Y.C. Li, D. Zhou, Y. Sun, M.A.T. Nguyen, M. Terrones, T.E. Mallouk, J. Am. Chem. Soc. 138 (2016) 5143–5149.
[41] J. Kim, S. Kwon, D.-H. Cho, B. Kang, H. Kwon, Y. Kim, S.O. Park, G.Y. Jung, E. Shin, W.-G. Kim, H. Lee, G.H. Ryu, M. Choi, T.H. Kim, J. Oh, S. Park, S.K. Kwak, S.W. Yoon, D. Byun, Z. Lee, C. Lee, Nat. Commun. 6 (2015) 8294.
[42] D. Lee, B. Lee, K.H. Park, H.J. Ryu, S. Jeon, S.H. Hong, Nano Lett. 15 (2015) 1238–1244.
[43] V. León, A.M. Rodriguez, P. Prieto, M. Prato, E. Vázquez, ACS Nano 8 (2014) 563–571.
[44] J. Li, D. Gao, J. Wang, S. Miao, G. Wang, X. Bao, J. Energy Chem. 24 (2015) 608–613.
[45] C. Tan, Z. Luo, A. Chaturvedi, Y. Cai, Y. Du, Y. Gong, Y. Huang, Z. Lai, X. Zhang, L. Zheng, X. Qi, M.H. Goh, J. Wang, S. Han, X.J. Wu, L. Gu, C. Kloc, H. Zhang, Adv. Mater. 30 (2018) 1705509.
[46] J. Hong, Z. Hu, M. Probert, K. Li, D. Lv, X. Yang, L. Gu, N. Mao, Q. Feng, L. Xie, J. Zhang, D. Wu, Z. Zhang, C. Jin, W. Ji, X. Zhang, J. Yuan, Z. Zhang, Nat. Commun. 6 (2015) 6293.
[47] S. Bertolazzi, J. Brivio, A. Kis, ACS Nano 5 (2011) 9703–9709.
[48] K. Liu, J. Feng, A. Kis, A. Radenovic, ACS Nano 8 (2014) 2504–2511.
[49] J. Xie, J. Zhang, S. Li, F. Grote, X. Zhang, H. Zhang, R. Wang, Y. Lei, B. Pan, Y. Xie, J. Am. Chem. Soc. 135 (2013) 17881–17888.
[50] L. Lin, N. Miao, Y. Wen, S. Zhang, P. Ghosez, Z. Sun, D.A. Allwood, ACS Nano 10 (2016) 8929–8937.
[51] S. Min, G. Lu, J. Phys. Chem. C 116 (2012) 25415–25424.
[52] X. Geng, W. Sun, W. Wu, B. Chen, A. Al-Hilo, M. Benamara, H. Zhu, F. Watanabe, J. Cui, T. Chen, Nat. Commun. 7 (2016) 10672.
[53] Q. Tang, D.-E. Jiang, ACS Catal. 6 (2016) 4953–4961.
[54] Y.-X. Pan, H.-P. Cong, Y.-L. Men, S. Xin, Z.-Q. Sun, C.-J. Liu, S.-H. Yu, ACS Nano 9 (2015) 11258–11265.
[55] S. Min, G. Lu, J. Phys. Chem. C 116 (2012) 19644–19652.
[56] U. Maitra, U. Gupta, M. De, R. Datta, A. Govindaraj, C.N.R. Rao, Angew. Chem. Int. Ed. 52 (2013) 13057–13061.